

Spatial mapping of the brain metabolome lipidome and glycome

Received: 24 August 2023

Accepted: 23 April 2025

Published online: 12 May 2025



Harrison A. Clarke^{1,2,11}, Xin Ma^{1,2,3,11}, Cameron J. Shedlock^{1,2,11}, Terryamar Medina^{1,2}, Tara R. Hawkinson^{1,2}, Lei Wu^{1,2}, Roberto A. Ribas^{1,2}, Shannon Keohane^{1,2}, Sakthivel Ravi^{1,2,4,5,6}, Jennifer L. Bizon^{4,5,7}, Sara N. Burke^{4,5,8}, Jose Francisco Abisambra^{1,2,4,5,6,9}, Matthew E. Merritt¹, Boone M. Prentice¹⁰, Craig W. Vander Kooi¹, Matthew S. Gentry^{1,2,12}, Li Chen^{1,2,12} & Ramon C. Sun^{1,2,5,12} ✉

Metabolites, lipids, and glycans are fundamental but interconnected classes of biomolecules that form the basis of the metabolic network. These molecules are dynamically channeled through multiple pathways that govern cellular physiology and pathology. Here, we present a framework for the simultaneous spatial analysis of the metabolome, lipidome, and glycome from a single tissue section using mass spectrometry imaging. This workflow integrates a computational platform, the Spatial Augmented Multiomics Interface (Sami), which enables multiomics integration, high-dimensional clustering, spatial anatomical mapping of matched molecular features, and metabolic pathway enrichment. To demonstrate the utility of this approach, we applied Sami to evaluate metabolic diversity across distinct brain regions and to compare wild-type and Ps19 Alzheimer's disease (AD) mouse models. Our findings reveal region-specific metabolic demands in the normal brain and highlight metabolic dysregulation in the Ps19 model, providing insights into the biochemical alterations associated with neurodegeneration.

Metabolomics^{1–3}, lipidomics^{4,5}, and glycomics^{6–8} are three distinct facets of omics methodologies, each offering a unique window into the connected and complex biochemical processes collectively known as the metabolic network. The current state of these fields lacks a unified, integrated analyses that offer a broad overview of the interconnected metabolic landscape. The development of an integrated spatially resolved metabolomics, lipidomics, and glycomics is crucial for advancing our knowledge of biological systems and has the potential to transform our understanding of the complex tissue metabolic

heterogeneity, uncover novel hypotheses for the etiology of a range of metabolic disorders. Nevertheless, the development of such integrated approaches is challenged by the inherent differences in physicochemical properties and analytical requirements of each molecular class such as size, solubility and charge.

Matrix-assisted laser desorption/ionization (MALDI) mass spectrometry imaging emerged as a powerful tool for spatially resolved multiomics analysis, offering the possibility to overcome major limitations associated with pooled sample analysis^{9,10}. Individual

¹Department of Biochemistry & Molecular Biology, College of Medicine, University of Florida, Gainesville, FL, USA. ²Center for Advanced Spatial Biomolecule Research, University of Florida, Gainesville, FL, USA. ³Department of Biostatistics College of Public Health and Health Professions & College of Medicine, University of Florida, Gainesville, FL, USA. ⁴Department of Neuroscience, University of Florida, Gainesville, FL, USA. ⁵Evelyn F. and William L. McKnight Brain Institute, University of Florida, Gainesville, FL, USA. ⁶Center for Translational Research in Neurodegenerative Disease (CTRND), University of Florida, Gainesville, FL, USA. ⁷Center for Addiction Research and Education, University of Florida, Gainesville, FL, USA. ⁸Institute on Aging, University of Florida, Gainesville, FL, USA. ⁹Brain Injury Rehabilitation and Neuroresilience (BRAIN) Center, University of Florida, Gainesville, FL, USA. ¹⁰Department of Chemistry, University of Florida, Gainesville, FL, USA. ¹¹These authors contributed equally: Harrison A. Clarke, Xin Ma, Cameron J. Shedlock. ¹²These authors jointly supervised this work: Matthew S. Gentry, Li Chen, Ramon C. Sun. ✉e-mail: ramonsun@ufl.edu

developments in spatial-metabolomics¹¹, -lipidomics^{12–14}, and -glycomics^{15–19} methodology are underway even at the single cell level^{20,21}. To this end, recent advances in MALDI imaging have enabled multiplexed analysis of diverse biomolecules²², such as the co-analysis of lipid, N-linked glycans and proteins, or N-linked glycans and storage carbohydrates such as glycogen by optimizing sample preparation, enzyme application, matrix selection, and instrumental parameters^{23–26}. These developments have poised MALDI imaging for broad adaptation in metabolism research, as they facilitate the acquisition of comprehensive and spatially resolved omics datasets. Further, the complexity and high dimensional nature of the datasets calls for the need of a robust computational pipeline to extract actionable and biologically relevant information for hypothesis generation¹⁷. An integrated workflow combining metabolomics, lipidomics, and glycomics from a single tissue section would offer unprecedented insights into the spatial and heterogeneous metabolic landscape of mammalian tissues, driving the next wave of metabolism research in health and diseases.

In this study, we present an experimental-computational workflow for the integration of spatial metabolomics, lipidomics, and glycomics datasets from a single mouse brain section. Our minimally destructive sequential sample preparation strategy enables the collection of sub-mesoscale spatial datasets for metabolites, lipids, and glycans while preserving spatial integrity. Furthermore, we leverage the Spatial Augmented Multiomics Interface (Sami) framework to perform advanced clustering and pathway analyses. This approach facilitates the identification of spatially resolved molecular patterns and key metabolic pathways across brain regions, providing actionable insights for investigators using a reductionist approach to dissect metabolism at the regional and cellular level. The triple-omics workflow not only enhances the resolution and scope of spatial biomolecular profiling but also accelerates hypothesis generation for spatial biology research. We anticipate that this platform will be widely adopted in metabolism research, enabling the discovery of novel molecular associations and driving the next wave of spatially resolved studies focused on understanding metabolic pathways in complex biological systems.

Results

A Workflow for spatial triple-omics by mass spectrometry imaging

The application of spatial metabolome, lipidome, and glycome on a single tissue section would present a multitude of benefits, primarily in maintaining the spatial continuity of the original tissue micro-environment and conserving tissue resources^{27–30}. A spatially resolved multi-omics approach facilitates a more holistic understanding of the metabolic network underpinning tissue heterogeneity and biology. Using a mouse brain as a model, we successfully acquired multiomics data from a single tissue section (Fig. 1). A single 10 μm thick brain section coated with N-(1-naphthyl) ethylenediamine dihydrochloride (NEDC) matrix was first subjected to sequential spatial metabolome and lipidome scans using MALDI mass spectrometry imaging (Fig. 1A). NEDC matrix and negative ionization mode are used for both spatial metabolome³¹ and lipidome³² analyses. Due to differences in ion optics tuning required for optimal transmission of low m/z metabolites ($< 500\ m/z$) and higher m/z lipids ($500–1500\ m/z$), metabolomics and lipidomics are performed as two separate runs (see methods, Supplemental Fig. 1). Following spatial lipidome imaging, the NEDC matrix was removed, and the tissue was fixed, then by Peptide - N-Glycosidase F (PnGase F) and Isoamylase digestion to release complex carbohydrates for spatial glycome and glycogen analysis^{30,31}. Spatial glycomics was performed in positive mode using α -cyano-4-hydroxycinnamic acid (CHCA) as the ionization matrix (Fig. 1A). We annotated metabolites, lipids, glycogen, and N-glycans through monoisotopic mass, isotope pattern, and matching through MetaboScape as well as from our own library^{17,33} and previously published assignments^{11,34,35} (Supplemental Dataset 1). We successfully demonstrated acquisition spatial images for molecular features in all three omics classes from both coronal and sagittal mouse brain sections (Fig. 1B). These include metabolites, lipids, and glycans with unique spatial distributions among different regions of a coronally or sagittally cut mouse brain (Fig. 1B). This method allows for a more holistic perspective of the metabolic network of the tissue and combines three omic analyses on a single tissue section.

To assess the reproducibility of the workflow, we performed spatial lipidomics on a sagittal brain section and compared it to lipidomics following metabolomics from an immediate adjacent brain section (Supplemental Fig. 2). Initial assessment revealed overall lower ion abundance in the total ion spectra in lipidomics following metabolomics compared to the lipidomics-only analysis as expected (Supplemental Figs. 2A, B). Despite the observed lower overall ion abundance between the spectra, the relative ratios of different m/z corresponding to lipid features have remained consistent. For

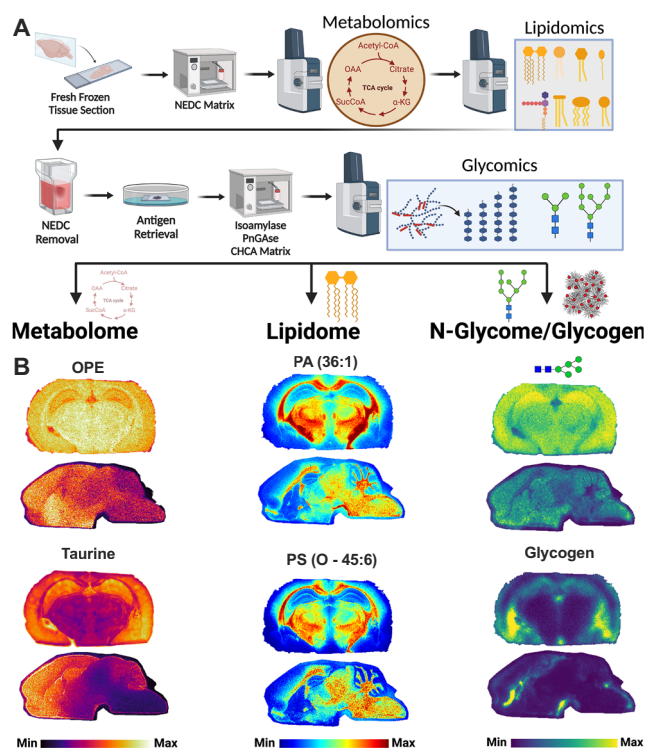


Fig. 1 | High-content spatial imaging of metabolome, lipidome, and glycome in a single mouse brain tissue. **A** Workflow for the sequential spatial analysis of the metabolome, lipidome, and glycome in mouse brain tissue sections using MALDI imaging. The process initiates with the slicing of fresh frozen mouse brains into 10 μm thick sections, either coronal or sagittal, followed by the application of the NEDC matrix for initial metabolite and lipid imaging. The same tissue sections are subsequently processed for glycomics analysis, involving isoamylase and PnGase F treatments before the application of the CHCA matrix, facilitating the visualization of complex carbohydrates like N-glycans and glycogen. Created in BioRender. Sun, R. (2025) <https://BioRender.com/k02u528>. **B** Spatial heatmaps/ion images that highlight the distribution of select biomolecules identified during the MALDI imaging of metabolome, lipidome, and glycome ($n = 2$, 1 for coronal section and 1 for sagittal section). The images represent both coronal and sagittal sections of mouse brains and are generated from the same tissue section following the workflow outlined in panel a. Biomolecule of interest is labeled above each heatmap/ion image, including o-phosphoethanolamine (OPE), Phosphatidic Acid (PA) (36:1), Taurine, Phosphatidylserine (PS) (O-45:6), and Glycogen. Color scale is not absolute but is relative to the highest local concentration of the biomolecule within each specific image, allowing for spatial visualization within the sample but not between different biomolecules or samples.

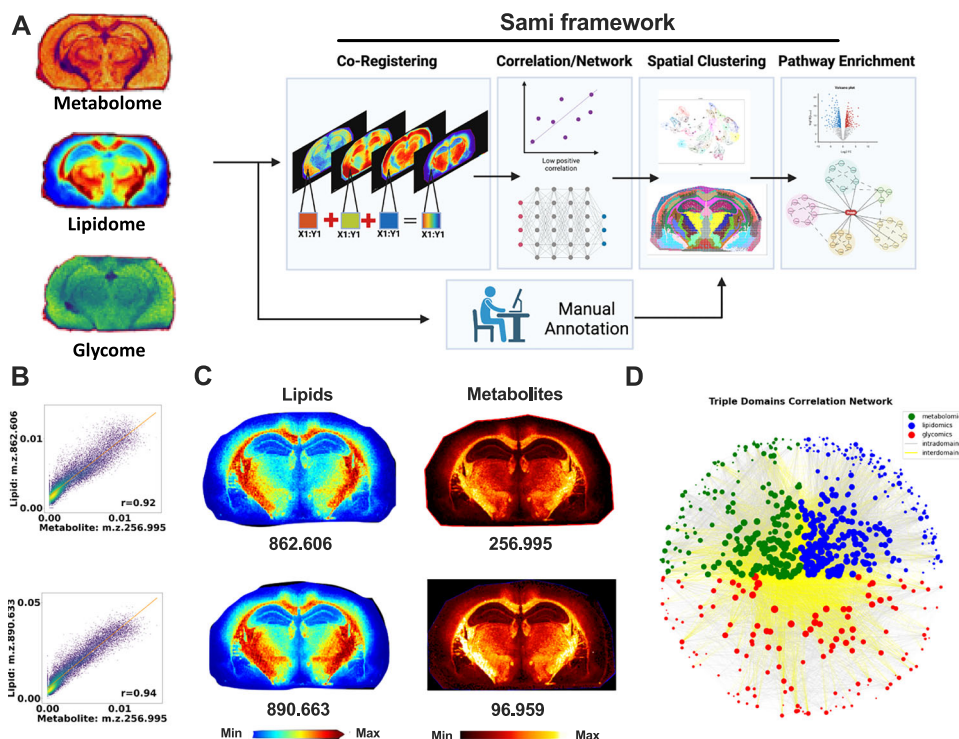


Fig. 2 | Spatial augmented multiomics interface (Sami) framework. **A** Sami computational framework: integration and spatial analysis of metabolomic, lipidomic, and glycomic data. The process begins with the co-registration of individual omics datasets, utilizing their spatial coordinates. Following this, correlation networks are established to identify low and high positive correlations between molecules, which then undergo spatial clustering to reveal the molecular architecture of the tissue. The final phase involves pathway enrichment analysis, which is complemented by manual annotation for data interpretation. Created in BioRender. Sun, R. (2025) <https://BioRender.com/f55v050>. **B** Scatter plots showing the strong Pearson correlation coefficient between paired metabolome and lipidome datasets after multiomics integration, demonstrating the quantitative relationship

between these two omics layers. **C** Paired spatial heatmap images of selected lipids and metabolites, such as 862.606 m/z and 256.995 m/z , reveal the distribution similarities between these molecules within the brain tissue. The color scale indicates the relative abundance from minimum (blue) to maximum (red). The monoisotopic masses and annotations are provided beneath each heatmap. The color scale corresponds to the highest pixel intensity detected for each individual biomolecule in each respective brain region. **D** Network analysis depicting the intricate intra- and interdomain connections of the integrated multiomics dataset. The metabolome (green), lipidome (blue), and glycome (red) nodes are connected within their respective domains (intradomain) by grey lines, while interdomain connections across different omic layers are shown in yellow.

example, the relative ratio for PI (38:4), LPE (22:6), and PE (38:4) when normalized to PE (40:6) remains consistent between both assays (Supplemental Fig. 2C). This is further highlighted as these lipids from both assays displayed similar spatial distribution after normalization to PE (40:6). It is worth noting that PS (40:6) showed a slight reduction even after normalization to PE (40:6), but the spatial distribution remain consistent between the two assays. Further, in parallel, we performed a similar comparison for glycomics. We again observed overall lower ion abundances in the glycomics analysis after metabolomics/lipidomics (Supplemental Figs. 3A, B), but the spatial distribution as well as ratios of glycans in the pixel-by-pixel analyses remained consistent between the two assays (Supplemental Fig. 3C). Collectively, these data demonstrate that while relative ion abundance decreases by performing the sequential workflow, the ratio of molecular features and spatial distribution within each assay remains relatively consistent and would have minimal impact spatial biological interpretation. To further demonstrate that metabolomics should be performed before lipidomics, we performed another control experiment with metabolomics after lipidomics scans (in reverse order), metabolomics performed after lipidomics analysis shown major reductions in ion abundance across the board, however, many metabolites such as aspartic acid and N-acetyl-L-aspartic acid still trend lower even after normalization (Supplemental Figs. 4A–C). It is worth noting that we observed a reduction in ion abundance from repeat sampling in both lipid and glycan scans as part of the sequential workflow. However, this reduction appears to occur consistently

across the m/z range, preserving the relative ratios of lipids and glycans as well as their spatial distributions, as demonstrated by comparisons to single-method scans.

Co-registering and integration of spatial multiomics datasets

With $>10^5$ pixels scanned per biological sample, the translation of MALDI multiomics datasets into actionable information to aid hypothesis-driven research presents a significant computational challenge. Recognizing this critical need, we developed a bioinformatic pipeline termed Spatial Augmented Multiomics Interface (Sami) that performs multiomics integration, high dimensionality reduction and clustering, spatial clustering, annotation, and pathway enrichment in one platform for the comprehensive analysis of spatial metabolome, lipidome, and glycome datasets (Fig. 2A). The first step of Sami is to perform multiomics integration, which consolidates the disparate biological features of metabolomics, lipidomics, and glycomics data into a singular, harmonized input suitable for high-dimensionality and pathway analyses (Fig. 2A). The smartbeam3 laser technology within the MALDI instrument registers x/y coordinates of the laser shots and preserve a unified x and y coordinates for each pixel across each omics modalities. By cross-referencing the x and y coordinates, Sami processing can determine the exact spatial location of each pixel in all datasets, effectively superimposing these multiple layers of omics information on a single spatial metadata location.

To test the degree of fit, the x and y coordinates were cross-referenced using enhanced correlation coefficient (ECC) for geometric

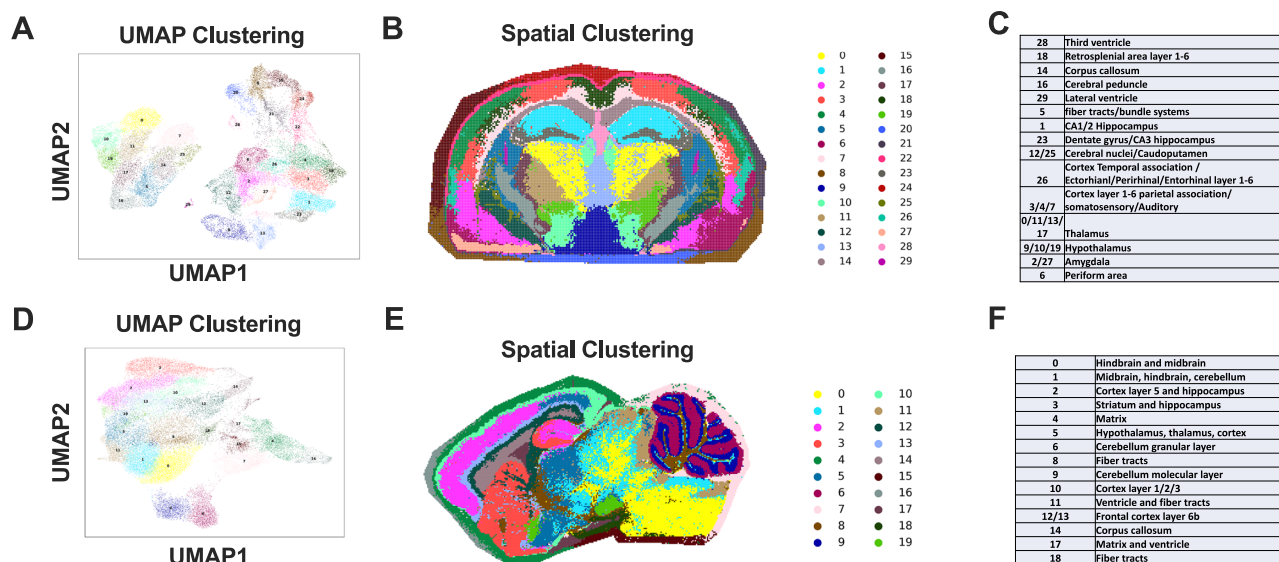


Fig. 3 | Spatial dimensionality reduction, and manual annotation in brain tissues. **A** Application of high-dimensionality reduction via UMAP on a dataset derived from a coronal brain section that has been processed through a triple-omics workflow. The UMAP plot visualizes the clustering of multidimensional omics data into a two-dimensional space, facilitating the identification of distinct clusters within the brain tissue. **B** The subsequent spatial clustering map displays the localized distribution of these clusters based on the precise x and y coordinates captured by the MALDI imaging laser spots. Each color on the map corresponds to a specific cluster, with the legend on the right side denoting the cluster numbers. **C** The clusters are then manually annotated with their respective anatomical

regions by a neuropathologist using the Allen Brain Atlas as a reference. **D** Similar to panel a, a UMAP plot presents the high-dimensionality reduction of omics data obtained from a sagittal brain section subjected to the same triple-omics workflow, delineating the diverse molecular landscapes across different brain structures. **E** The subsequent spatial clustering map displays the localized distribution of these clusters based on the precise x and y coordinates captured by the MALDI imaging laser spots. Each color on the map corresponds to a specific cluster, with the legend on the right side denoting the cluster numbers. **F** Each cluster number is again correlated with specific anatomical regions identified in the sagittal section, guided by manual annotation by a neuropathologist with the Allen Brain Atlas.

transformation, which is a statistical measure of imaging alignment employed by computer vision³⁶. We leveraged these data by selecting m/z features in overlapping m/z regions of two modalities (i.e., 400–700 m/z range between metabolomics and lipidomics) (Supplemental Fig. 5A). Ion images of four m/z ratios were tested that included on-tissue and off-tissue m/z features (Supplemental Fig. 5B). We performed ECC analysis of both ion images from different modalities after pixel-to-pixel matching, or manually shifting one modality either 1, or 5 pixels in both x and y directions to demonstrate miss-alignment (Supplemental Fig. 5C). Direct pixel-to-pixel matching yielded a near perfect ECC score of 0.95 (out of 1), while shifting pixels by 1 or 5 registers resulted in a score of 0.82 and 0.67, respectively (Supplemental Fig. 5D). Finally, we demonstrated the glycan signals overlay with the original tissue scan to show spatially unique regions and accurate co-registration (Supplemental Figure 6). These data support that direct pixel-to-pixel integration provides excellent alignment between different modalities.

Successful integration opens the opportunity for additional analyses such as correlation and network analyses across modalities. We found a number of features in different modalities shown high levels co-expression, their abundance and spatial distribution (Fig. 2B, C). For example, 256.995 m/z from metabolomics and 862.606 m/z from the lipidomics analysis exhibit high levels of spatial co-expression identified after multiomics integration (Fig. 2B). Finally, we demonstrated multiomics integration through inter and intra domain connectivity via network analysis (Fig. 2D). Network analysis reveals connectivity between metabolites across different modalities, indicating effective integration of pixels across the three omics runs. This integration will enable co-analysis of metabolomics, lipidomics, and glycomics datasets, providing a systems-level understanding of metabolic networks and allowing for downstream pathway analysis (Fig. 2D). Collectively, our data support the generation of a single robust, integrated, single spatially resolved dataset from three different omics modalities.

High dimensionality reduction, spatial clustering, and annotation

High-dimensionality reduction as part of the Sami framework serves as a powerful strategy to distill high dimensional MALDI MSI datasets to actionable and manageable information (Fig. 3). To this end, UMAP has the highest computational efficiency without sufficing dimensionality reduction clustering comparing to other methods^{37–39} and has been demonstrated to perform well in MALDI imaging datasets⁴⁰. Therefore, we tested whether performing UMAP clustering on the integrated triple-omics dataset is beneficial over individual UMAP analysis of single modalities. Indeed, UMAP analysis of the triple-omics dataset (metabolomics, lipidomics, and glycomics) encompassed unique clusters present in individual UMAP analysis of individual modalities (Supplemental Figure. 7), highlighting the importance of combined triple-omics analysis. Further, we confirmed that combining all three modalities did not reduce clustering efficiency comparing to single modality using the Silhouette score⁴¹ (Supplemental Figure. 7E). Upon performing the spatial clustering of the coronal brain, we found that the spatial clusters correspond well with the anatomically distinct brain regions similar to previous finding^{42–44} (Fig. 3B). We manually annotated each spatial cluster using Mouse Brain Atlas from the Allen Institute as a guide⁴² (Fig. 3B, C). This comparison revealed a high degree of similarity between the spatial clusters and the recognized brain regions, offering evidence of the biological relevance of UMAP clustering that relates to the biochemistry of the brain. To confirm this finding, we performed similar UMAP clustering and spatial annotation in the sagittal brain section as well (Fig. 3D–F). Similar to the coronal brain section, UMAP spatial clustering revealed multiple brain anatomical regions (Fig. 3F). The number of clusters displayed by UMAP in Sami can be adjusted by modifying parameters such as the clustering resolution, number of nearest neighbors and minimum distance, which influence the number and size of clusters observed in the results (Supplemental Figure. 8).

To further enhance the utility of the spatial multiomics map, we then established a reference multiomics feature set for the annotation of brain regions. Selected features for represented clusters are shown as Radial trees and density plots (Supplemental Figs. 9A, B). Annotated clusters can serve as a reference guide, aiding in the assignment and interpretation of multiomics features across different studies. To confirm the robustness of the annotations derived through Sami, we first performed spatial triple-omics in a separate coronal brain section (test brain) and performed unsupervised spatial clustering (Supplemental Figs. 10A–D). Each cluster in the test brain were matched to one cluster in the original reference brain section through feature matching (See “Methods”), resulting in a supervised cluster matching. Using this methodology, the annotation from the clusters in the reference brain section can be directly used for the test brain section (Supplemental Figs. 10A–G). We then further tested this method in four different sagittal mouse brain sections, and the method provided excellent matching for sagittal brain sections as well among all clusters. We were able to match 100% of all clusters to the reference brain (Supplemental Figure. 10E). Further we used Jaccard index to assess the degree of matching for each individual cluster, we found an average of 0.8 (max 1) Jaccard index score (range 0.55–0.89) for all clusters tested indicating high degree of similarity among matched clusters and high reproducibility in our methods (Supplemental Figs. 10G and Supplemental Dataset 2).

Spatially resolved pathway enrichment analysis with Sami

Subsequent to spatial clustering and annotation, Sami performs pathway analysis, a key step to distill down large omics datasets and to provide actionable next steps for hypothesis generating research. First, we tested whether there are metabolic differences between intra-brain regions highlighted by clustering analysis within the WT brain. We performed differential expression analysis by comparing each cluster against the rest of the clusters as illustrated by volcano plots (Fig. 4A); Based on differential expression analysis, the top 50 annotated multiomics features of each cluster exhibiting significant alterations were selected for metabolic pathway enrichment analysis via the MetaboAnalyst 3.2 pipeline embedded in Sami. Specifically, we conducted enrichment analyses using the Small Molecule Pathway Database (SMPDB)⁴⁵, within MetaboAnalyst 3.2 pipeline (Supplemental Figure. 11). An example of pathway enrichment analysis for the cluster corresponds to the CA3 region of the hippocampus, which predominantly consists of excitatory pyramidal neurons, highlights the Citric Acid Cycle and Glutamate Metabolism as the top two enriched pathways (Fig. 4B, C). In contrast, the top two enriched pathways for the Corpus Callosum showed unique enrichment for gluconeogenesis, Warburg effect, and glycolysis (Supplemental Figure. 11). These findings demonstrate that multi-omics integration combined with spatial clustering can reveals region-specific metabolic signatures within the brain. In addition, Sami can also export metabolites that are over or underrepresented in each pathway (see “methods”), as well calculating a score for overall directionality of each enriched pathway to facilitate data interpretation. For example, the metabolites enriched for the citric acid cycle are aconitate, malate, pyruvate, succinate, and ADP, and it is considered down regulated overall based on Sami output (supplemental Dataset 3).

To further demonstrate the utility of the spatial pathway enrichment analysis by Sami, we performed spatial metabolomics, lipidomics, and glycomics and applied Sami to probe the metabolic dysfunction between WT and the mouse model of tauopathy (Ps19). The Ps19 Alzheimer’s disease mouse model expresses the human *MAPT* (P301S) mutant tau gene under the prion promoter, leading to progressive tau pathology, neurodegeneration, and cognitive deficits resembling frontotemporal dementia⁴⁶. This model is widely used to study tauopathies, therapeutic interventions, and mechanisms of tau-driven neurodegeneration⁴⁷. We perform triple-omics following Sami

analysis that include co-UMAP clustering followed by pathway mapping between 9-month-old female WT and Ps19 mice (Fig. 5A–C). All three omics modalities were used for UMAP clustering similar to above, and since both WT and Ps19 mouse brains were clustered together, both brains give rise to the same (20) non-overlapping clusters (Supplemental Figure. 12). In addition, similar brain regions can be matched to the same cluster (visualized by color). i.e., cerebellum, pink; cortex, blue; corpus callosum, brown. We performed metabolic pathway enrichment (Ps19/WT) using the cluster correspond to the isocortex and cerebellum of both WT and Ps19 mouse brains. In the isocortex we identified changes in citric acid cycle, warburg effect, carnitine synthesis, and transfer of acetyl groups to mitochondria as major pathways altered in the cortex of mouse model of tauopathy (Fig. 5D–F). In contrast, cerebellum in the tauopathy model shown changes in Starch and sucrose metabolism, Glycerolipid metabolism, glycolysis, and triacylglycerol biosynthesis (Supplemental Figure. 13). It is worth noting that metabolites such as glucose-6-phosphate, glucose, and glycogen are classified as part of starch and sucrose metabolism by the Kegg pathway.

While both the citric acid cycle and the Warburg effect were highlighted in both intra-brain (Fig. 4B) and inter-brain regional analyses (Fig. 5E). Similarly, aconitate, malate, pyruvate, succinate were all identified as altered in both analyses, however, directionality analysis suggests that citric acid cycle is down in intra-brain analysis, but is shown as up in the inter-brain regional analyses between WT and Ps19 mice (Supplemental Dataset 4). We further demonstrate this, we extracted pixel-by-pixel relative abundance data for metabolites associated with these pathways in the intra-brain analysis of the WT brain and the WT vs. Ps19 comparison in the isocortex. Notably, although both pathways were enriched, the changes at the metabolite level differed. For example, in the CA3 region, citrate and aconitate levels were increased, while malate, succinate, and GSH levels were decreased relative to the rest of the brain (Fig. 4C). In contrast, in the Ps19 isocortex, citrate and aconitate were decreased, and malate was increased compared to WT (Fig. 5G). Additionally, glycogen, identified through glycomics analysis, was significantly elevated in the Ps19 mouse isocortex. To validate these spatial multi-omics findings, we performed multiplexed immunofluorescence analysis targeting key enzymes in the citric acid cycle and the metabolite glycogen, which is part of the starch and sucrose metabolism pathway. This analysis revealed significant reductions in the protein levels of citrate synthase, aconitase, and isocitrate dehydrogenase in the Ps19 brain (Fig. 5H). Conversely, glycogen levels were significantly increased in the Ps19 cortex, as confirmed using a previously validated anti-glycogen antibody^{39,40}. These results support the findings from spatial multi-omics analyses and highlight the utility of integrating spatially resolved multi-omics data with targeted validation approaches for mapping region-specific metabolic changes in both healthy and diseased brains.

Discussion

Metabolomics, lipidomics, and glycomics are corner stone techniques driving biological discovery in the last several decades^{48–50}. In this study, we present a roadmap to perform simultaneous assessments of the metabolome, lipidome, and glycome from a single tissue section. This represents a major advancement compared to traditional pooled omics analyses, providing a broad and comprehensive assessment of the metabolic landscape or network. Our approach overcomes several limitations of conventional pooled methods, offering insights into the spatial distributions of a wide array of biomolecules, multimodal and integrated analysis, thereby fostering a nuanced understanding of the metabolic processes within complex tissue microenvironments. In addition, by direct sampling of whole tissue sections, the triple-omics workflow minimizes sample handling (such as tissue pulverization) and fractionation steps (phase separation)⁵¹ of pooled omics methods. The entire pipeline can be completed within a span of 72 h when

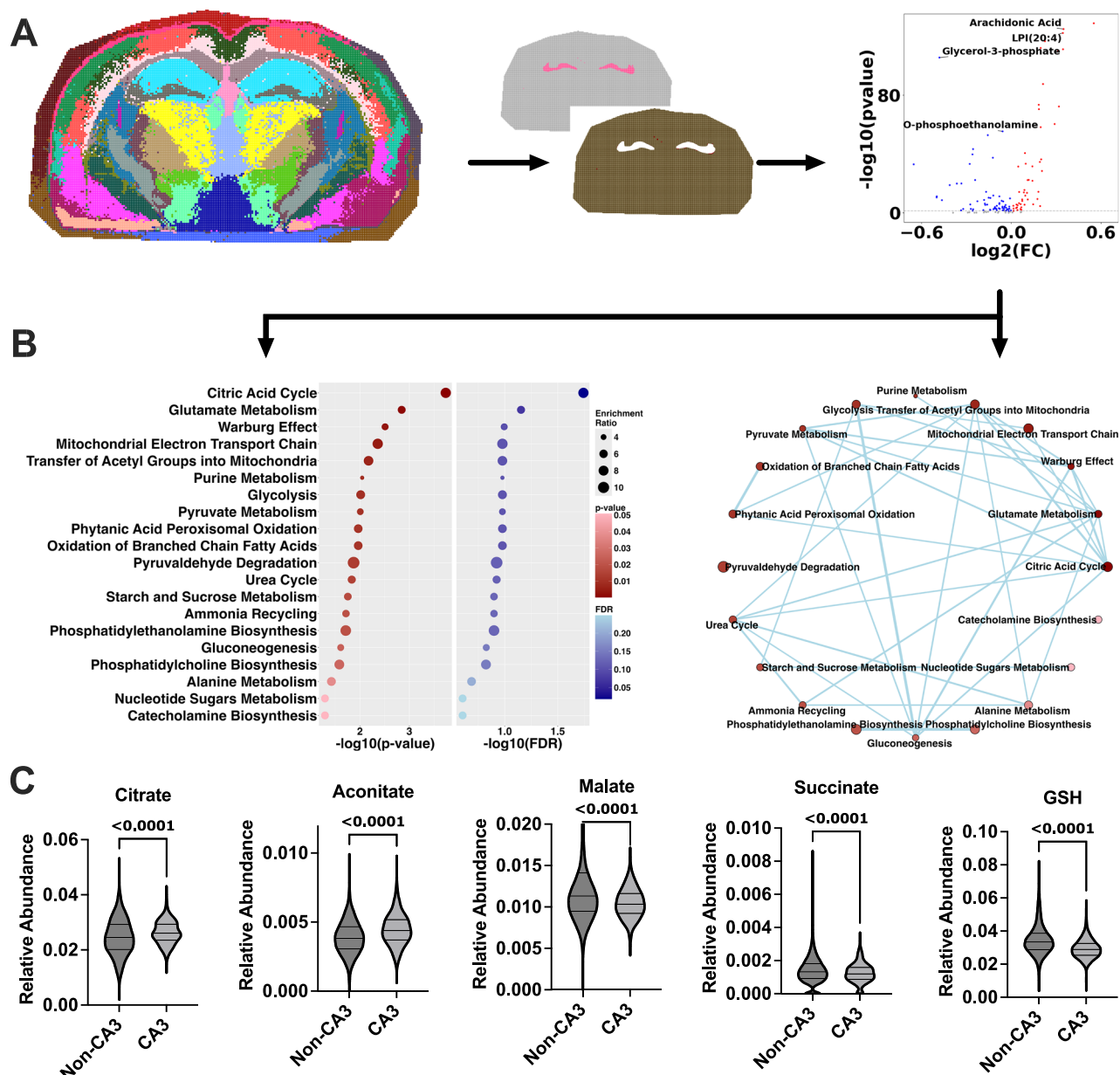


Fig. 4 | Metabolic diversity in distinct brain regions of a normal mouse brain.

A Spatial clustering map depicting anatomical regions in a normal mouse brain, with a focus on the CA3 region, compared to the rest of the brain. A corresponding volcano plot elucidates the significant metabolic differences between the CA3 area and the rest of the brain, using adjusted p -value threshold of 0.05 to denote significance (Wilcoxon Rank-Sum test, Benjamini-Hochberg (BH) procedure for multiple comparison). Metabolomic features that are elevated in the CA3 region are indicated in red, while those that are decreased are shown in blue. **B** Metabolic pathway enrichment analysis, constructed using the MetaboAnalyst 3.2 R package integrated within the Sami, pinpoints the specific metabolic pathways that are significantly enriched in the CA3 region (Wilcoxon Rank-Sum test, Benjamini-

Hochberg (BH) procedure for multiple comparison). The analysis is complemented by a metabolic network visualization, which connects the metabolic pathways identified by pathway enrichment analysis with more than 25% share metabolites, enhancing our understanding of the metabolic interplays and diversity within the CA3 region. Nodes represent biochemical pathways. The size of the nodes and color correlate with the degree of enrichment. **C** relative abundance of metabolites changed in the citric acid cycle, bar graphs represent pixel by pixel data from CA3 ($n = 527$ pixels) and non-CA3 ($n = 20,000$ pixels) regions of the same brain ($n = 1$). (mean \pm SEM; p -values indicated; two-tailed t -test). Source data are provided as a Source Data file.

imaging at a resolution of 50 μ m and Sami offers a promising platform for high-throughput omics studies for the future.

In addition, we also report the robust computational framework of Sami, a series of tools customized and designed specifically to optimize multimodal datasets produced by triple-omics MALDI imaging runs. Sami's ability to integrate three different modalities and reduce high-dimensional data into spatial clusters that correlate with brain anatomy. This is followed by metabolic pathway enrichment analyses for unique spatial clusters in both healthy and disease brain

tissues. Collectively, the combination of triple-mics workflow and Sami represents a leap forward in the quest to understand metabolic diversity of different brain regions. It is worth noting that these data are by nature hypothesis generating in nature and can be further tested in human and genetic mouse models by targeting specific metabolic pathways. One finding from our study is the efficacy of metabolism as a classifier of brain regions, a concept that could drive our understanding of brain functionality and neurological disorders^{52–54}. The differential metabolic profiles unveiled through our

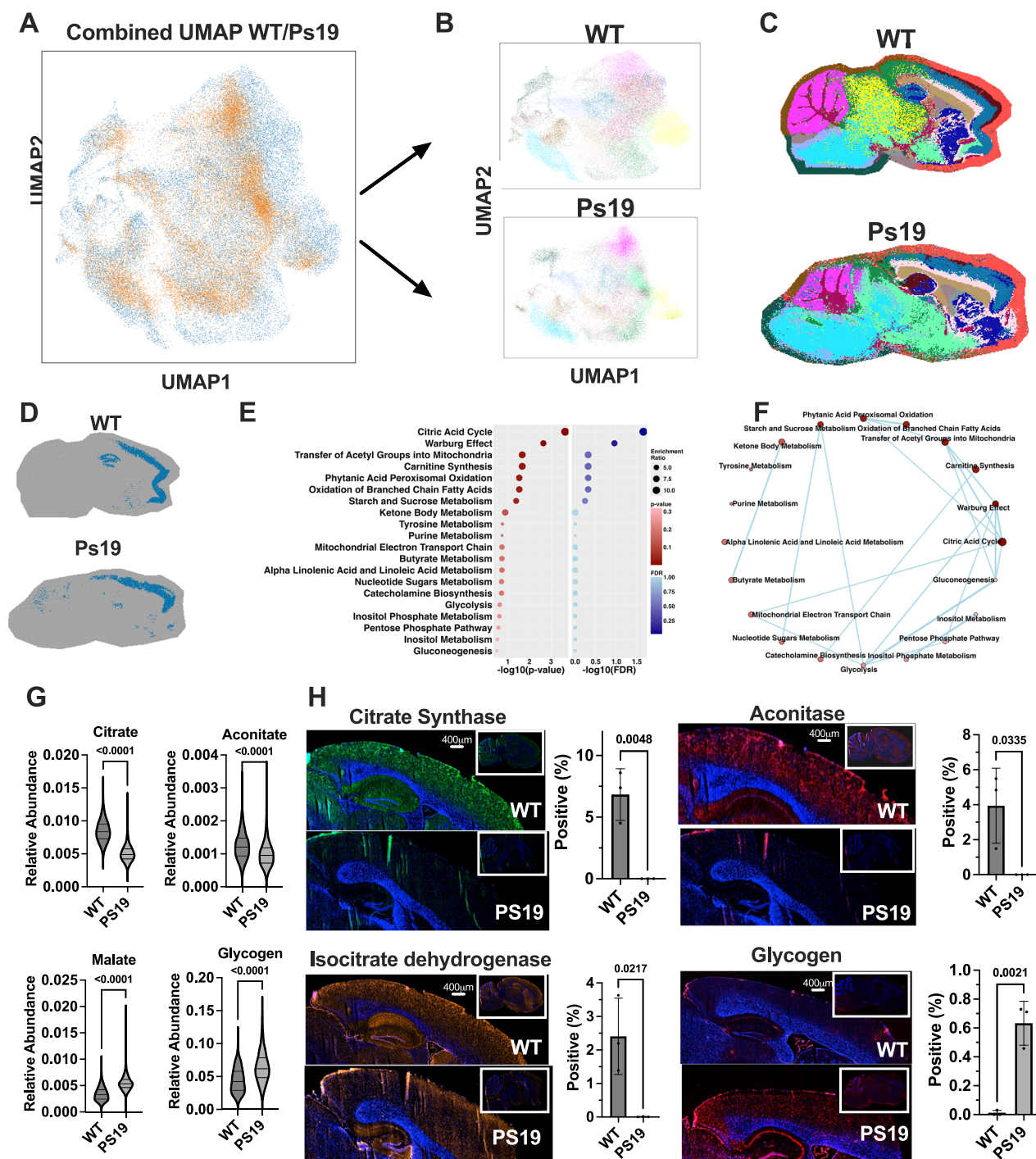


Fig. 5 | Pathway enrichment analysis for Ps19 and WT mouse brains. **A** UMAP plot displays the integration of data from Ps19 (brown) and matched WT (blue) sagittal mouse brains ($n = 1$ each). **B** Separate UMAP plots for Ps19 and WT brains are shown, detailing the full range of clusters within each brain type. **C** Spatial clustering maps overlay UMAP clusters onto the anatomical structures of both Ps19 and WT mouse brains. **D** Spatial UMAP plots highlight a specific cluster corresponding to the frontal cortex region in sagittal sections of both Ps19 and WT brains. **E** Pathway enrichment analysis, using the MetaboAnalyst 3.2 R package integrated within Sami, identifies metabolic pathways that are differentially enriched in the Ps19 brain as compared to WT (Hypergeometric test, Benjamini-Hochberg (BH) procedure for multiple comparison). **F** A metabolic network diagram connects the enriched pathways, highlighting the relationships and potential dysregulation occurring in Ps19 brains relative to WT. Nodes represent biochemical

pathways. The network graphically summarizes the interconnected pathways with more than 25% overlapping metabolites. **G** Relative abundance of metabolites changed in the Citric acid cycle, bar graphs represent pixel by pixel data from the isocortex region of the WT ($n = 2043$ pixels) and Ps19 ($n = 2295$ pixels) brains. **H** Representative immunofluorescence staining images show the localization of Citrate Synthase, Aconitase, Isocitrate Dehydrogenase, and Glycogen in brain sections from WT and Ps19 mice, scale bar = $400\ \mu\text{m}$. Whole brain image is in the insert on the top right. Each row displays the enzyme or glycogen marker in both WT (top) and Ps19 (bottom) sections, with the corresponding quantification bar graphs (% positive and positive area) presented on the right (mean \pm SEM, $n = 3$ WT and Ps19 animals; p -values indicated; two-tailed t -test). Source data are provided as a Source Data file.

pathway enrichment analyses, demarcate specific brain regions, emphasizing the spatial heterogeneity of metabolic processes within the brain. For example, The CA3 region of the hippocampus is predominantly composed of excitatory pyramidal neurons. Our pathway enrichment and network analysis highlight multiple pathways converging to mitochondrial function, presumed to be associated with pyramidal neurons. e., citric acid cycle is a core component of mitochondrial metabolism, which is critical for providing the energy required to modulate pyramidal neuronal activity and excitability^{55,56}. Notably, glutamate, the primary excitatory neurotransmitter in the brain⁵⁷, is synthesized from the Citric Acid Cycle intermediate α -ketoglutarate. This metabolic linkage emphasizes the dual role of mitochondrial metabolism in both supporting the energy demands of neurons and providing the substrates necessary for neurotransmitter synthesis. Similarly, the cluster corresponding to corpus callosum are enriched for gluconeogenesis, Warburg effects, and glycolysis. It has been demonstrated the preference of glycolysis (i.e. Warburg effect) by different cell types within the corpus callosum, i.e., astrocytes⁵⁸, oligodendrocytes⁵⁹, and microglia⁶⁰. Together, these pathway analyses highlighted the potential unique metabolic demands within different regions of the brain. These findings take the first step in improving understanding of brain metabolism, paving the way for novel research avenues into the complex interplay between brain function and metabolic activity.

Sami offers spatial pathway enrichment analysis for uncovering region-specific metabolic signatures within the brain or metabolic dysregulation between WT and disease mouse brains. However, the lack of directional information from pathway enrichment highlights the importance of metabolite-level analysis. For instance, while the citric acid cycle was highlighted in both intra-regional analysis within the WT brain and WT/Ps19 isocortex analyses, the specific metabolite changes were distinct, with opposing alterations observed in citrate, aconitate, and malate. These findings underscore the necessity of extracting and evaluating the most significantly altered metabolites driving pathway enrichment to pinpoint the exact metabolic alterations in each context. Detailed metabolite-level analyses are critical to planning hypothesis-driven experiments that will advance these observations into actionable insights, such as manipulating unique metabolic enzymes in the Ps19 mouse model to improve neurodegeneration.

The current study presents the Sami workflow, which integrates metabolomics, lipidomics, and glycomics from a single tissue section into a unified data analysis pipeline designed for hypothesis-generating research. Using WT and Ps19 mouse brains as examples, this pipeline focuses on exploring regional heterogeneities, including intra-regional differences within WT brains and inter-regional comparisons between WT and Ps19 brains. During the sequential MALDI scan, there will be a preferential loss of lower-abundance ions, which can be mitigated through additional targeted workflows by optimizing acquisition parameters and focusing on specific molecular features based on the users interest. Strategies to address this issue should include increasing laser energy, adjusting pixel sizes, or modify quadrupole settings to boost ion intensity in targeted analyses. One limitation of this workflow is that it does not yet provide cellular-level insights. Emerging multimodal imaging approaches, such as the integration of MALDI imaging with cellular functions through techniques like Imaging Mass Cytometry (IMC)⁶¹, CODEX⁶², Xenium⁶³, VISIUM (spatial transcriptomics)⁶⁴, are beginning to bridge this gap. Additionally, the development of MALDI immunohistochemistry holds significant promise for advancing cellular annotation on a single tissue section⁶⁵. Future methodological developments will aim to assign metabolomic, lipidomic, and glycomics data to specific cellular annotations, enabling deeper biological insights into tissue function and pathology. Additional future development will focus on expanding omics feature coverage such as extracellular matrix proteins, o-linked

glycans, and other small molecule metabolites⁶⁶ and improving laser raster size of 5 μ m (required better co-registration algorithms), which is near single-cell level^{67,68}. We anticipate 5 μ m multiomics imaging coupled to cellular annotation would offer deeper insights into metabolic cross talk and heterogeneity at the single-cell level. Additionally, while our current annotations focus on the brain, future work should seek to identify metabolic classifiers for other tissues, such as liver, kidney, and lung, and extend these analyses to metabolic diseases such as cancers, neurological disorders, and inborn errors of metabolism. The Sami framework is designed to accommodate these updates, functioning as an expandable system that can be updated as new improvements emerge. In conclusion, our data show that Sami is a powerful tool for multiomics research; we envision an even brighter future as we continue to refine and expand this innovative platform.

Methods

Chemicals, reagents, antibodies, and cell lines

High-performance liquid chromatography (HPLC)-grade acetonitrile, ethanol, methanol, water, trifluoroacetic acid (TFA), N-(1-Naphthyl) ethylenediamine dihydrochloride (NEDC), and recombinant isoamylase were purchased from Sigma-Aldrich. α -cyano-4-hydroxycinnamic acid (CHCA) matrix was purchased from Cayman Chemical. Histological-grade xylenes were purchased from Spectrum Chemical. Citraconic anhydride for antigen retrieval was obtained from Thermo Fisher Scientific. Recombinant PNGaseF Prime was obtained from N-Zyme Scientific (Doylestown, PA, USA). Bruker IntelliSlides (Bruker Daltonics). The following antibodies were used: Alexa Fluor® 488 anti-Citrate synthetase (1:200, Abcam, ab197488); Alexa Fluor® 647 anti-Aconitase 2 (1:200, Abcam, ab198050); Alexa Fluor® 594 anti-Isocitrate dehydrogenase (1:200, Abcam, ab311797); mouse anti-glycogen (IV58B6) (1:500, in-house hybridoma). Secondary antibody used are: Alexa Fluor 647-conjugated anti-mouse (1:200, Invitrogen, A21238).

Mouse models

Mice were housed in a climate-controlled environment with a 14 (light)/10 (dark) hours light/dark cycle with temperature (18–23 °C) and humidity (50–60%) control. Water and solid diet provided *ad libitum* throughout the study (Tekad #2018). Wild-type (WT) C57BL/6J mice and Ps19 mice were purchased from Jackson Laboratory. The University of Florida Institutional Animal Care and Use Committee has approved all of the animal procedures under the protocol number IACUC202200000586.

Sample collection and preparation

Mice were euthanized by cervical dislocation and decapitation. Immediately following euthanasia, the brains were surgically resected within 30 s. Mouse brains were dissected into two hemispheres coronally to expose regions to be scanned by MALDI. The brain tissue was first rinsed in 1x Phosphate-Buffered Saline (PBS) and subsequently rinsed twice with deionized water. The rinsed tissues were blotted dry, then slow-frozen over isopentane chilled with dry-ice for seven minutes, according to previously established protocols^{69,70}, to ensure tissue stability and optimal preservation of analytes. Post-freezing, the samples were stored at –80 °C until further processing.

MALDI MSI tissue preparation

The frozen tissues were sectioned by a cryostat at an ambient temperature of –15 °C, chilled to –20 °C to prepare for cutting. A Leica CM1860 cryostat was utilized to obtain coronal sections of 10 μ m thickness. Tissues were mounted onto a frozen Leica chuck using Optimal Cutting Temperature (OCT) compound as a binding agent for sectioning. The brains were shaved until the target region was exposed. The sections were then thaw-mounted onto a Bruker IntelliSlides and stored at –80 °C for future use. Post-sectioning, the tissue

samples were fixed by dehydration using a vacuum desiccator for one hour. The slides were processed sequentially for small molecules, lipids, glycans and glycogen for triple omics data acquisition by MALDI imaging.

Matrix and enzyme application for imaging

Following an hour of vacuum desiccation, N-(1-Naphthyl) ethylenediamine dihydrochloride (NEDC) matrix was applied and sprayed using an HTX M5 pneumatic sprayer, using a matrix solvent of HPLC-grade methanol and water in a 70:30 mix. Then slides were sprayed with 7 mg/mL NEDC matrix in 70% methanol solvent, using 14 passes at a rate of 0.06 mL/min, a 3 mm offset, and a velocity of 1200 mm/min. The conditions were maintained at 30 °C and 10 psi, with a heated tray set at 50 °C. Following this stage, metabolites and lipids were imaged on the slides using respective instrument methods and a standardized flexImaging (v7.2).mis file to ensure consistent pixel integration across all omic runs. After lipid imaging, the slides were removed from the instrument and the NEDC matrix was stripped off using an ice-cold, 100% methanol wash for 5 min, and fixed overnight with 10% (v/v) neutral buffered formalin (37% Formaldehyde and 1x PBS). The protocol for CHCA matrix and enzyme application for glycans and glycogen was previously described^{53,71,72}. Briefly, the tissue sections were dehydrated and rehydrated through a sequence of immersions once in 70% ethanol (1 min) and twice in water (3 min each). Antigen retrieval at 95 °C for 25 min, with citraconic anhydride buffer prepared using 25 μ L citraconic anhydride in 50 mL water, and pH adjusted to 3 using hydrochloric acid (HCl). An HTX spray station (HTX) was used to coat the slide with a 0.2 mL aqueous solution of isoamylase (3U/slide) and PNGase F (20 mg total/slide). The spray nozzle was heated to 45 °C with a spray velocity of 900 mm/min. Following enzyme application, slides were incubated at 37 °C for 2 h in a humidified chamber, and dried in a vacuum desiccator prior to matrix application (0.04 g CHCA in 5.7 mL 50% acetonitrile/50% water and 5.7 μ L 25%TFA) applied with HTX sprayer.

MALDI imaging

All MALDI MSI experiments were performed on a Bruker timsTOF fleX using a 46 μ m \times 46 μ m laser raster to produce 50 μ m \times 50 μ m pixels. All image acquisition and setup are performed through the autopilot feature with FlexImaging 6.0 to avoid human errors. All omic runs require a standardized flexImaging .mis file to be used as a consistent masked template denoting the regions for imaging. To generate this file, slides were scanned, and high-resolution .tif files were imported to flexImaging to manually mask the regions of tissue for imaging. To optimize post-run data processing and ensure consistent pixel integration, the same .mis file was employed for all runs, paired with the appropriate omic-specific method. The metabolomics run initiated the omics workflow, during which the first and only flexImaging.mis file was created. This file was subsequently used for all future runs, ensuring aligned pixel integration across conditions while modifying the method to suit the respective omic. Small molecule metabolite imaging was conducted in negative ion mode with the following detailed settings: MS1 scan, scan range from m/z 20–750, negative polarity, summation rate mode, and a rate value of 544. The laser configuration included 50 μ m \times 50 μ m pixels from a 46 μ m \times 46 μ m raster scan range, 90% laser power, 1 burst of 396 shots, a frequency of 10,000 Hz, and a transfer configuration of 30 V MALDI plate offset, –60 V deflection 1 delta, 200 Vpp Funnel 1 RF, 200 Vpp Funnel 2 RF, and 200 Vpp Multipole RF. Collision energy was set to 7 eV, with a collision RF of 700 Vpp. Lipidomic imaging was performed immediately after the metabolomics run, maintaining negative ion mode. The lipidomics MS1 scan parameters included a scan range of m/z 300–2000, negative polarity, and a similar summation rate mode. The laser was configured identically with 50 μ m \times 50 μ m pixels from a 46 μ m \times 46 μ m raster scan range, 80% laser power, 1 burst of

300 shots, a frequency of 10,000 Hz, and corresponding transfer settings. Collision energy and collision RF parameters mirrored those used in the metabolomics imaging. Glycomic imaging data were collected after preparing the slides as described and imaging in positive ion mode with these settings: MS1 scan, scan range from m/z 700–4000, positive polarity, summation rate mode, and a rate value of 210. The laser configuration featured 50 μ m \times 50 μ m pixels from a 46 μ m \times 46 μ m raster scan range, 37% laser power, 1 burst of 320 shots, a frequency of 10,000 Hz, and transfer parameters of 50 V MALDI plate offset, 70 V deflection 1 delta, 500 Vpp Funnel 1 RF, 500 Vpp Funnel 2 RF, and 500 Vpp Multipole RF. Collision energy was set to 10 eV, with a collision RF of 4000 Vpp.

Peak annotations and export

MALDI imaging data analysis was conducted using MetaboScape® software for exporting MS data acquired in negative ion mode into the.srd format, followed by data upload from Bruker Scisils™ Software Solutions.T-ReX® 2D algorithm was applied, focusing exclusively on MS data. Subsequent analysis incorporated parameters such as an intensity threshold of 500, speckle width and height of 3, and a maximum of 200 speckles, with ion deconvolution targeting [M-H][–], [M+Cl][–], and [M-H₂O][–] ions. Annotation employed a hierarchical approach, starting with a curated list of 7k MS1 mammalian endogenous metabolites, followed by lipid identification using the MCube spectral library integrated into MetaboScape. Further annotation utilized a combination of in-house and public spectral libraries, including an in-house library of over 50,000 endogenous metabolites (curated through standards), the latest HMDB Metabolite Library, MoNA, MassBank, FiehnLib LipidBlast library, MetaboBASE® Personal Library 2023, the Bruker Sumner MetaboBASE®, and NIST 2022. Annotation accuracy was ensured through stringent m/z tolerances (5–10 ppm), mSigma values (25–250), and comprehensive parallel library searches, with unannotated features explored via SmartFormula for molecular formula prediction. Results were exported in.mca format to Scisils for peak width refinement and ion image quality assessment before final export in.csv format. Export to a pixel-by-pixel tabular format was performed using the SCiLS lab R package and corresponding API (available from Bruker). Peak area was used and no normalization method was applied at this stage. Exported tabular metadata for each omics MALDI imaging can be found as part of the submission files.

Immunofluorescence

Immediately adjacent tissue section from the MALDI imaging analysis is used for immunofluorescent analysis. Fresh frozen tissue sections were fixed for 30 min at room temperature in 1% paraformaldehyde and were rehydrated in a series of graded ethanol (95%, 70%, 50%) until water was used. Subsequently antigen retrieval was performed by immersing sections in 10 mM citrate buffer (pH 6.0) in Water Bath for 1 h at 96 °C then cool at room temperature for 30 min. Sections were blocked for 1 h in 2% normal goat serum and 5% (w/v) Bovine Serum Albumin (BSA) in 0.05% TBS/Ocyl β -D-Glucopyranoside. Primary antibodies were incubated overnight at 4 °C, while secondary antibodies were incubated for 1 h at room temperature. All images are acquired using the Akoya Phenolmager slide scanner.

Data co-registration and integration

Untargeted spatial metabolomics, lipidomics, and glycomics datasets, derived from MALDI imaging, were first loaded into SCiLS Lab software to check image quality and assess overall data integrity. Features with an m/z count > 400 were exported for further analysis. These selected features were exported to a tabular format using the SCiLS Lab software's API. Exported individual tabular triple omics data files are accessible as supplementary materials. Following the export, each omics file was individually co-registered based on their X and Y coordinate information embedded within the tabular file type. For the

actual data integration, the co-registered omics files were converted from tabular data files (.csv) to annotated data matrices (.h5ad), normalized by total ion count and log-transformation, and merged into a single annotated data matrix by **csv2h5ad()** and **pooldata()** functions in a custom script (preprocess.py) as part of the Spatial Augmented Multiomics Interface (Sami) framework (available at <https://github.com/XinBiosats/SAMI>). The final output was a comprehensive annotated data matrix containing the spatially aligned m/z features from the metabolomics, lipidomics, and glycomics datasets. Once the data integration was complete, we proceeded with further analyses including feature correlation analysis, high-dimensional clustering, spatial mapping, cluster marker identification, and pathway enrichment analysis. More detailed methods for each of these analyses follow in subsequent sections.

Correlation analysis

The correlation analysis was executed using the Pearson correlation coefficient, with a specific lipid m/z value serving as the reference variable. The **calculate_corr()** function was employed to compute the correlation coefficients between the reference lipid m/z feature and all the other metabolomic features in the integrated dataset across all available pixels. Following the acquisition of correlation coefficients, scatter plots were produced using **corr_plot()** to visually interpret these correlations. Each pair of features was plotted, with the m/z value of metabolite on the x-axis and the m/z value of lipid on the y-axis. Correlation coefficient (r) is calculated and presented on each graph. Both **calculate_corr()** and **corr_plot()** functions are available in custom Python script “correlation.py” in Sami.

Network analysis of inter- and intra-domain omics interactions

The elucidation of interactions between and within each omics domain was achieved via a comprehensive network analysis. Firstly, the **DataFrame.corr()** function in the “pandas” Python library version 1.5.3 was used to calculate the Pearson correlation coefficients among all pairs of m/z features, both within and between each omics domain. This provided a comprehensive matrix of correlation values that capture the potential inter- and intra-omic associations. Next, Pearson correlation larger than 0.5 on a pixel scale was retained. The **corr_network()** function based on “networkX” Python library 3.0 was then utilized to transform the correlation matrix into a network graph, with m/z features represented as nodes and significant correlations as edges between them. Nodes were annotated to indicate the omics domain to which the feature belongs, providing a clear picture of the interplay among metabolomics, lipidomics, and glycomics features. Both **DataFrame.corr()** and **corr_network()** functions are available in custom Python script “correlation.py” in Sami.

High dimensional clustering and spatial mapping

High-dimensional clustering was performed in two steps: 1) dimension reduction and 2) clustering based on the reduced dimensions. To reduce the dimensionality of the feature space while preserving critical information, **scanpy.pp.pca()** in “scanpy” Python library 1.9.1 (n_comps = 20) was used to perform principal component analysis (PCA) to retain top 20 principal components (PCs). Subsequently, the Leiden algorithm was employed on the 20 PCs to assign cluster memberships to pixels by using **scanpy.tl.leiden()** function in “scanpy” Python library 1.9.1 (resolution = 1.4). The uniform manifold approximation and projection (UMAP) from **scanpy.tl.umap()** in “scanpy” Python library 1.9.1 is used to visualize the clusters. Spatial mapping of these clusters was performed by linking the clusters back to their original spatial coordinates (X and Y) within the sample. This allowed us to visualize the spatial distribution of these omics clusters and for exploring their spatial relationships. Three functions perform high-dimensional clustering and spatial mapping are available in custom script clustering.py in Sami: **plot_umap_cluster()** function

generates UMAP and spatial mapping in parallel: **plot_cluster()** function creates the spatial mapping only; **plot_select_cluster()** function selectively plots clusters of interest in the spatial mapping. To relate these spatial clusters with known anatomical structures, we annotated each spatial cluster against the brain regions presented in the Allen Institute Mouse Brain Atlas (Available from atlas.brain-map.org). This was accomplished by overlaying the coordinates of our clusters with the spatial coordinates of the brain regions in the Allen Mouse Brain Atlas. Any spatial cluster that coincided with the coordinates of a particular brain region in the Atlas was annotated with the name of that region.

To demonstrate the benefits of multi-omics integration for clustering, we evaluate the clustering results of single-omics and multi-omics data using the Silhouette Score. The Silhouette Score is a widely used metric to assess the quality of clustering by measuring the cohesion and separation within and between clusters. For each data point i , the Silhouette Score $s(i)$ is defined as:

$$s(i) = \frac{b(i) - a(i)}{\max(a(i), b(i))} \quad (1)$$

where $a(i)$ is the average distance of sample i to all other points in its own cluster and $b(i)$ is the average distance of sample i to points in the nearest neighboring cluster. We calculated the average Silhouette Score across all data points as the final clustering evaluation score. The Silhouette Score ranges from -1 to 1, where a higher score indicates better clustering quality, as the data points are more compact within their clusters and better separated from other clusters. The Silhouette Score was computed using the **silhouette_score()** function from sklearn library in Python.

Volcano plot, density plot and circular plot

Volcano plot was implemented by **volcano_plot()** function. Specifically, each point represents an m/z feature with its log2 fold change on the x-axis and negative log10 p -value on the y-axis. Red points represent overrepresentation, blue points represent underrepresentation, and gray points indicate non-significant pixels. To visualize the distribution and relative abundance of each m/z feature across different clusters, we generated density plots using **density_plot()** function, which is similar to the ones utilized in single-cell RNA sequencing (scRNA-seq) analyses. These plots depict the difference of pixel abundance of a particular m/z marker in a specific cluster compared to its pixel abundance in other clusters, providing an insight into the cluster-specific distribution of these omics entities. Furthermore, top 5 markers of selected clusters from three different omics were displayed as a circular tree. All three functions are available in custom Python script “marker.py” in Sami.

Supervised clustering with reference tissue section

To validate that the protocol and computational pipeline was robust for different tissue sections, we generated a new triple omics dataset from MALDI imaging performed on a fresh brain section. Similar to the previous steps, spatial clusters and cluster-specific markers were delineated based on the new dataset. We denoted the previous tissue section as the “reference” and the new tissue section as the “validation section”. To evaluate if the two tissue sections share a similar clustering pattern for reproducible finding, we used the cluster-specific markers to align the clusters between the two sections as the cluster IDs were generated randomly. For each cluster in the validation section, we computed the number of shared markers (50 markers for each omics set, a total of 150 markers for triple omics) between the reference clustering and each cluster in the discovery/validation section. This process was completed by **cluster_mapping()** function in clustering.py in Sami. We defined the matched cluster in the discovery section as the cluster with the highest number of common markers.

Cluster marker identification

A differential abundance analysis was conducted to identify cluster-specific m/z by contrasting the abundance of each m/z feature in a specific cluster to the abundance of the same m/z feature in the rest of the clusters combined. A Wilcoxon Rank-Sum test is performed to compare the abundance in the two groups. The resulting p -values were adjusted for multiple testing to control the false discovery rate (FDR). For each cluster, the top 50 statistically significant features (Adjusted p -value < 0.05) ranked by absolute \log_2 transformed fold change are selected as the cluster-specific markers. These markers constituted a unique signature for each cluster, serving as identifiers in subsequent analyses such as metabolic pathway enrichment analysis. **Findmarkers()** function for cluster marker identification is available in custom Python script “marker.py” in Sami.

Pathway enrichment analysis

Pathway enrichment analysis was done using top 50 features of each cluster, which can be annotated and exhibiting significant alterations (Adjusted p -value < 0.05 and ranked by absolute fold change) were selected for metabolic pathway enrichment analysis. The pathway enrichment analysis was performed via the MetaboAnalystR 3.2 pipeline embedded in Sami. This pipeline employs a hypergeometric test for over-representation analysis. Due to the absence of a comprehensive database encompassing all three - metabolome, lipidome, and glycome—for pathway mapping, we conducted separate enrichment analyses: one for combined metabolomics and glycomics via the Small Molecule Pathway Database (SMPDB)⁴⁵, and another for lipids using the lipid library integrated within MetaboAnalyst. After identifying significant pathways via selected markers, we assessed their regulation by computing the \log_2 fold change (\log_2FC) of all measured compounds within each pathway. A pathway is classified as up-regulated if $\log_2FC > \text{threshold}$, down-regulated if $\log_2FC < -\text{threshold}$, and neutral if it falls within $[-\text{threshold}, \text{threshold}]$, where the threshold (e.g., 0.1) is predefined. The function **plot_dot()** was used to show the enriched pathways. The function **plot_bar_for_direction()** was utilized to display up-regulated and down-regulated pathways separately. We further explore and visualize the relationship of cluster-specific metabolic pathways by performing a pathway network analysis. In the pathway network, nodes represent metabolic pathways and two nodes are connected if the corresponding two pathways have more than 25% shared features among combined sets. The network was generated by **pathway_network()** function based on Networkx package. All functions are available in custom script pathway.py in Sami (available at <https://github.com/XinBiostats/SAMI>).

Reporting summary

Further information on research design is available in the Nature Portfolio Reporting Summary linked to this article.

Data availability

All MALDI files in imzML format generated in this study are available at <https://sunlabresources.rc.ufl.edu>. All data supporting the findings of this manuscript will also be shared by the authors upon request. Source data are provided with this paper.

Code availability

Python code for Spatial Augmented Multiomics Interface (Sami) framework is deposited and available at <https://github.com/XinBiostats/SAMI>. <https://doi.org/10.5281/zenodo.15022515>. Example datasets in txt format are provided via <https://zenodo.org/records/15224641>.

References

- Lisec, J., Schauer, N., Kopka, J., Willmitzer, L. & Fernie, A. R. Gas chromatography mass spectrometry-based metabolite profiling in plants. *Nat. Protoc.* **1**, 387–396 (2006).
- Fiehn, O. Metabolomics—the link between genotypes and phenotypes. *Funct. genomics* **48**, 155–171 (2002).
- Gibney, M. J. et al. Metabolomics in human nutrition: opportunities and challenges. *Am. J. Clin. Nutr.* **82**, 497–503 (2005).
- Han, X. & Gross, R. W. Shotgun lipidomics: electrospray ionization mass spectrometric analysis and quantitation of cellular lipidomes directly from crude extracts of biological samples. *Mass Spectrom. Rev.* **24**, 367–412 (2005).
- Cajka, T. & Fiehn, O. Toward merging untargeted and targeted methods in mass spectrometry-based metabolomics and lipidomics. *Anal. Chem.* **88**, 524–545 (2016).
- Cummings, R. D. & Pierce, J. M. The challenge and promise of glycomics. *Chem. Biol.* **21**, 1–15 (2014).
- Wada, Y. et al. Comparison of the methods for profiling glycoprotein glycans—HUPO Human Disease Glycomics/Proteome Initiative multi-institutional study. *Glycobiology* **17**, 411–422 (2007).
- Ruhaak, L. et al. Glycan labeling strategies and their use in identification and quantification. *Anal. Bioanal. Chem.* **397**, 3457–3481 (2010).
- Caprioli, R. M., Farmer, T. B. & Gile, J. Molecular imaging of biological samples: localization of peptides and proteins using MALDI-TOF MS. *Anal. Chem.* **69**, 4751–4760 (1997).
- McDonnell, L. A. & Heeren, R. M. Imaging mass spectrometry. *Mass Spectrom. Rev.* **26**, 606–643 (2007).
- Wang, J. et al. MALDI-TOF MS imaging of metabolites with a N-(1-naphthyl) ethylenediamine dihydrochloride matrix and its application to colorectal cancer liver metastasis. *Anal. Chem.* **87**, 422–430 (2015).
- Zemski Berry, K. A. et al. MALDI imaging of lipid biochemistry in tissues by mass spectrometry. *Chem. Rev.* **111**, 6491–6512 (2011).
- Djambazova, K. V. et al. Resolving the complexity of spatial lipidomics using MALDI TIMS imaging mass spectrometry. *Anal. Chem.* **92**, 13290–13297 (2020).
- Zhang, H. et al. Single-cell lipidomics enabled by dual-polarity ionization and ion mobility-mass spectrometry imaging. *Nat. Commun.* **14**, 5185 (2023).
- Drake, R. R. et al. MALDI mass spectrometry imaging of N-linked glycans in cancer tissues. *Adv. cancer Res.* **134**, 85–116 (2017).
- Powers, T. W. et al. MALDI imaging mass spectrometry profiling of N-glycans in formalin-fixed paraffin embedded clinical tissue blocks and tissue microarrays. *PLoS one* **9**, e106255 (2014).
- Conroy, L. R. et al. Spatial metabolomics reveals glycogen as an actionable target for pulmonary fibrosis. *Nat. Commun.* **14**, 2759 (2023).
- Veličković, D., Veličković, M., O’Connor, C. L., Bitzer, M. & Anderton, C. The Impact of the Mass Analyzer and Tissue Section Thickness on Spatial N-Glycomics with MALDI-MSI. *J. Am. Soc. Mass Spectrom.* **36**, 823–828 (2025).
- Wei, X. & Li, L. Comparative glycoproteomics: approaches and applications. *Brief. Funct. genomics Proteom.* **8**, 104–113 (2009).
- Rappez, L. et al. SpaceM reveals metabolic states of single cells. *Nat. methods* **18**, 799–805 (2021).
- Tian, H. et al. Multimodal mass spectrometry imaging identifies cell-type-specific metabolic and lipidomic variation in the mammalian liver. *Developmental Cell* **59**, 869–881. e866 (2024).
- Black, A. P. et al. A novel mass spectrometry platform for multiplexed N-glycoprotein biomarker discovery from patient biofluids by antibody panel based N-glycan imaging. *Anal. Chem.* **91**, 8429–8435 (2019).
- Young, L. E. et al. In situ mass spectrometry imaging reveals heterogeneous glycogen stores in human normal and cancerous tissues. *EMBO Mol. Med.* **14**, e16029 (2022).
- Clift, C. L., Mehta, A., Drake, R. R. & Angel, P. M. Multiplexed Imaging Mass Spectrometry of Histological Staining, N-Glycan and Extracellular Matrix from One Tissue Section: A Tool for Fibrosis

- Research. In: *Multiplexed Imaging. Methods in Molecular Biology*. (ed Zamir, E.) **2350** (Humana, New York, NY, 2021).
25. Clift CL, Drake RR, Mehta A, Angel PM. Multiplexed imaging mass spectrometry of the extracellular matrix using serial enzyme digests from formalin-fixed paraffin-embedded tissue sections. *Anal Bioanal Chem.* **413**, 2709–2719 (2021).
 26. Denti, V. et al. Spatial multiomics of lipids, N-glycans, and tryptic peptides on a single FFPE tissue section. *J. Proteome Res* **21**, 2798–2809 (2022).
 27. Cornett, D. S., Reyzer, M. L., Chaurand, P. & Caprioli, R. M. MALDI imaging mass spectrometry: molecular snapshots of biochemical systems. *Nat. methods* **4**, 828–833 (2007).
 28. Bartolacci, C. et al. Targeting de novo lipogenesis and the Lands cycle induces ferroptosis in KRAS-mutant lung cancer. *Nat. Commun.* **13**, 4327 (2022).
 29. Sun, C. et al. Spatially resolved multi-omics highlights cell-specific metabolic remodeling and interactions in gastric cancer. *Nat. Commun.* **14**, 2692 (2023).
 30. Duhamel, M. et al. Spatial analysis of the glioblastoma proteome reveals specific molecular signatures and markers of survival. *Nat. Commun.* **13**, 6665 (2022).
 31. Chen, R. et al. High-salt-tolerance matrix for facile detection of glucose in rat brain microdialysates by MALDI mass spectrometry. *Anal. Chem.* **84**, 465–469 (2012).
 32. Wang, J., Wang, C. & Han, X. Enhanced coverage of lipid analysis and imaging by matrix-assisted laser desorption/ionization mass spectrometry via a strategy with an optimized mixture of matrices. *Analytica Chim. acta* **1000**, 155–162 (2018).
 33. Conroy, L. R. et al. In situ analysis of N-linked glycans as potential biomarkers of clinical course in human prostate cancer. *Mol. Cancer Res.* **19**, 1727–1738 (2021).
 34. Wang, G. et al. Analyzing cell-type-specific dynamics of metabolism in kidney repair. *Nat. Metab.* **4**, 1109–1118 (2022).
 35. Wang, L. et al. Spatially resolved isotope tracing reveals tissue metabolic activity. *Nat. Methods* **19**, 223–230 (2022).
 36. Evangelidis, G. D. & Psarakis, E. Z. Parametric image alignment using enhanced correlation coefficient maximization. *IEEE Trans. pattern Anal. Mach. Intell.* **30**, 1858–1865 (2008).
 37. Trozzi, F., Wang, X. & Tao, P. UMAP as a dimensionality reduction tool for molecular dynamics simulations of biomacromolecules: a comparison study. *J. Phys. Chem. B* **125**, 5022–5034 (2021).
 38. Allaoui, M., Kherfi, M. L. & Cheriet, A. Considerably Improving Clustering Algorithms Using UMAP Dimensionality Reduction Technique: A Comparative Study. In: *Image and Signal Processing. ICISP 2020. Lecture Notes in Computer Science* (eds El Moataz, A., Mammass, D., Mansouri, A., Nouboud, F.) **12119** (Springer, Cham, 2020).
 39. Hernández-Hernández, S. & Ballester, P. J. On the best way to cluster NCI-60 molecules. *Biomolecules* **13**, 498 (2023).
 40. Smets, T. et al. Evaluation of distance metrics and spatial autocorrelation in uniform manifold approximation and projection applied to mass spectrometry imaging data. *Anal. Chem.* **91**, 5706–5714 (2019).
 41. Rousseeuw, P. J. Silhouettes: a graphical aid to the interpretation and validation of cluster analysis. *J. computational Appl. Math.* **20**, 53–65 (1987).
 42. Sunkin, S. M. et al. Allen Brain Atlas: an integrated spatio-temporal portal for exploring the central nervous system. *Nucleic acids Res.* **41**, D996–D1008 (2012).
 43. Dong, H. W. et al. *The Allen reference atlas: A digital color brain atlas of the C57BL/6J male mouse*. (John Wiley & Sons Inc., 2008).
 44. Alexandrov, T. et al. Spatial segmentation of imaging mass spectrometry data with edge-preserving image denoising and clustering. *J. Proteome Res* **9**, 6535–6546 (2010).
 45. Frolkis, A. et al. SMPDB: the small molecule pathway database. *Nucleic acids Res.* **38**, D480–D487 (2010).
 46. Yoshiyama, Y. et al. Synapse loss and microglial activation precede tangles in a P301S tauopathy mouse model. *Neuron* **53**, 337–351 (2007).
 47. Iba, M. et al. Tau pathology spread in PS19 tau transgenic mice following locus coeruleus (LC) injections of synthetic tau fibrils is determined by the LC's afferent and efferent connections. *Acta neuropathologica* **130**, 349–362 (2015).
 48. Worley, B. & Powers, R. Multivariate analysis in metabolomics. *Curr. metabolomics* **1**, 92–107 (2013).
 49. Wenk, M. R. The emerging field of lipidomics. *Nat. Rev. Drug Discov.* **4**, 594–610 (2005).
 50. Hart, G. W. & Copeland, R. J. Glycomics hits the big time. *Cell* **143**, 672–676 (2010).
 51. Smith, L. et al. Important considerations for sample collection in metabolomics studies with a special focus on applications to liver functions. *Metabolites* **10**, 104 (2020).
 52. Camandola, S. & Mattson, M. P. Brain metabolism in health, aging, and neurodegeneration. *EMBO J.* **36**, 1474–1492 (2017).
 53. Sun, R. C. et al. Brain glycogen serves as a critical glucosamine cache required for protein glycosylation. *Cell Metab.* **33**, 1404–1417. e1409 (2021).
 54. Conroy, L. R., Hawkinson, T. R., Young, L. E., Gentry, M. S. & Sun, R. C. Emerging roles of N-linked glycosylation in brain physiology and disorders. *Trends Endocrinol. Metab.* **32**, 980–993 (2021).
 55. Groten, C. J. & MacVicar, B. A. Mitochondrial Ca²⁺ uptake by the MCU facilitates pyramidal neuron excitability and metabolism during action potential firing. *Commun. Biol.* **5**, 900 (2022).
 56. Stoler, O. et al. Frequency- and spike-timing-dependent mitochondrial Ca²⁺ signaling regulates the metabolic rate and synaptic efficacy in cortical neurons. *Elife*. **11**, e74606 (2022).
 57. Mattson, M. P., Dou, P. & Kater, S. B. Outgrowth-regulating actions of glutamate in isolated hippocampal pyramidal neurons. *J. Neurosci.* **8**, 2087–2100 (1988).
 58. Hertz, L., Peng, L. & Dienel, G. A. Energy metabolism in astrocytes: high rate of oxidative metabolism and spatiotemporal dependence on glycolysis/glycogenolysis. *J. Cereb. Blood Flow. Metab.* **27**, 219–249 (2007).
 59. Fünfschilling, U. et al. Glycolytic oligodendrocytes maintain myelin and long-term axonal integrity. *Nature* **485**, 517–521 (2012).
 60. Wang, L. et al. Glucose transporter 1 critically controls microglial activation through facilitating glycolysis. *Mol. Neurodegeneration* **14**, 2 (2019).
 61. Nunes, J. B. et al. Integration of mass cytometry and mass spectrometry imaging for spatially resolved single-cell metabolic profiling. *Nat. Methods* **21**, 1796–1800 (2024).
 62. Black, S. et al. CODEX multiplexed tissue imaging with DNA-conjugated antibodies. *Nat. Protoc.* **16**, 3802–3835 (2021).
 63. Ma, X. et al. Protocol for Xenium spatial transcriptomics studies using fixed frozen mouse brain sections. *STAR Protoc.* **5**, 103420 (2024).
 64. Vicari, M. et al. Spatial multimodal analysis of transcriptomes and metabolomes in tissues. *Nat. Biotechnol.* **42**, 1046–1050 (2024).
 65. Claes, B. S. et al. MALDI-IHC-guided in-depth spatial proteomics: targeted and untargeted MSI combined. *Anal. Chem.* **95**, 2329–2338 (2023).
 66. Wadie, B., Stuart, L., Rath, C. M. & Alexandrov, T. METASPACE-ML: Context-specific metabolite annotation for imaging mass spectrometry using machine learning. *Nat Commun.* **15**, 9110 (2024).
 67. Guenther, S., Römpf, A., Kummer, W. & Spengler, B. AP-MALDI imaging of neuropeptides in mouse pituitary gland with 5 µm spatial resolution and high mass accuracy. *Int. J. Mass Spectrom.* **305**, 228–237 (2011).

68. Zavalin, A., Yang, J., Hayden, K., Vestal, M. & Caprioli, R. M. Tissue protein imaging at 1 μ m laser spot diameter for high spatial resolution and high imaging speed using transmission geometry MALDI TOF MS. *Anal Bioanal Chem.* **407**, 2337–2342 (2015).
69. Juras, J. A. et al. In situ microwave fixation provides an instantaneous snapshot of the brain metabolome. *Cell Rep. Methods* **3**, 100455 (2023).
70. Stanback, A. E. et al. Regional N-glycan and lipid analysis from tissues using MALDI-mass spectrometry imaging. *STAR Protoc.* **2**, 100304 (2021).
71. Hawkinson, T. R. & Sun, R. C. Matrix-assisted laser desorption/ionization mass spectrometry imaging of glycogen in situ. *Mass Spectrometry Imaging of Small Molecules: Methods and Protocols*, 215–228 (2022).
72. Hawkinson, T. R. et al. In situ spatial glycomic imaging of mouse and human Alzheimer's disease brains. *Alzheimer's Dement.* **18**, 1721–1735 (2022).

Acknowledgements

This study was supported by National Institute of Health (NIH) grants R01AG066653, R01CA266004, R01AG078702, RM1NS133593, 1R01CA288696-01V-Scholar Grant, to R.C.S., R35NS116824 to M.S.G., R35GM142701 to L.C., T32HL134621 to H.A.C., 2T32HD043730-21 to C.J.S.

Author contributions

Conceptualization, R.C.S. Methodology, R.C.S. and L.C. and X.M.; Investigation, H.A.C., C.J.S., T.M., T.R.H., L.W., R.A.R., S.K., S.R., J.L.B., S.N.B., J.F.A., M.E.M., B.M.P., C.W.V. and M.S.G.; Writing – Original Draft, R.C.S.; Writing—Review & Editing, R.C.S., H.A.C., C.W.V., M.S.G.; Funding Acquisition, M.S.G., R.C.S.; Resources, M.S.G., R.C.S.; Supervision, L.C., R.C.S.

Competing interests

R.C.S. has research support and received consultancy fees from Maze Therapeutics. R.C.S. is a member of the Medical Advisory Board for Little Warrior Foundation and M.S.G. is a member of the science advisory board for Chelsea's Hope, Glut1-deficiency syndrome, and the adult polyglucosan body disease foundation. M.S.G. has research support and

research compounds from Maze Therapeutics, Valerion Therapeutics, Ionis Pharmaceuticals. M.S.G. also received consultant fees from Maze Therapeutics. The remaining authors declare no competing interests.

Additional information

Supplementary information The online version contains supplementary material available at <https://doi.org/10.1038/s41467-025-59487-7>.

Correspondence and requests for materials should be addressed to Ramon C. Sun.

Peer review information *Nature Communications* thanks Matei Banu, Alex Dickens, and the other, anonymous, reviewer(s) for their contribution to the peer review of this work. A peer review file is available.

Reprints and permissions information is available at <http://www.nature.com/reprints>

Publisher's note Springer Nature remains neutral with regard to jurisdictional claims in published maps and institutional affiliations.

Open Access This article is licensed under a Creative Commons Attribution-NonCommercial-NoDerivatives 4.0 International License, which permits any non-commercial use, sharing, distribution and reproduction in any medium or format, as long as you give appropriate credit to the original author(s) and the source, provide a link to the Creative Commons licence, and indicate if you modified the licensed material. You do not have permission under this licence to share adapted material derived from this article or parts of it. The images or other third party material in this article are included in the article's Creative Commons licence, unless indicated otherwise in a credit line to the material. If material is not included in the article's Creative Commons licence and your intended use is not permitted by statutory regulation or exceeds the permitted use, you will need to obtain permission directly from the copyright holder. To view a copy of this licence, visit <http://creativecommons.org/licenses/by-nc-nd/4.0/>.

© The Author(s) 2025